Supplementary information

Molecular Structure and Dielectric Anisotropy of Ethanol-Water Mixtures within Heterogeneous Graphene/silica Interface.

*Liangchen Mei, Zhijun Xu, Xiaoning Yang**

State Key Laboratory of Materials-Oriented Chemical Engineering,

College of Chemical Engineering,

Nanjing Tech University,

Nanjing 211816, China

Email: Yangxia@njtech.edu.cn

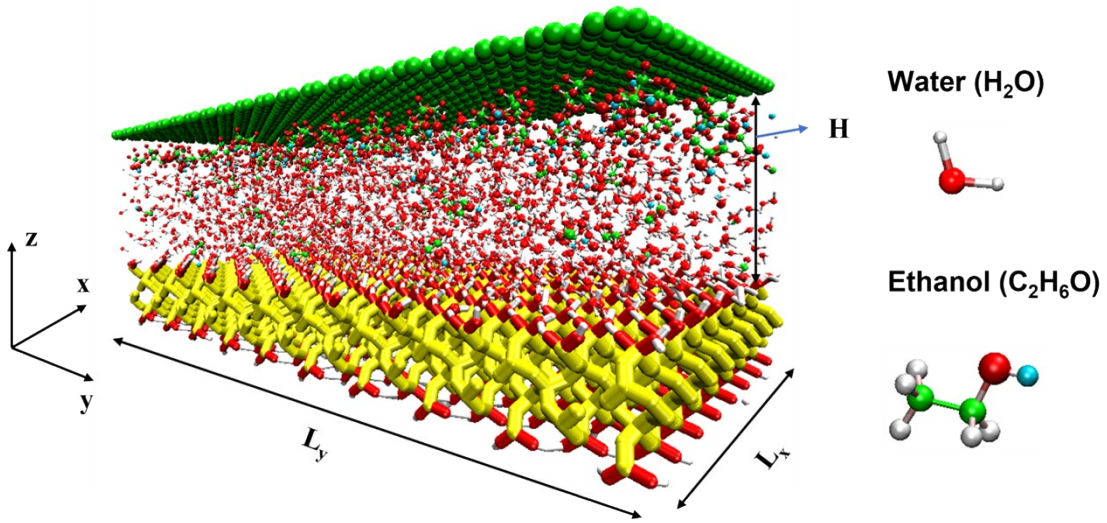

Fig. S1. The typical simulation system of an ethanol–water mixture confined between a graphene sheet and a fully hydroxylated bilayer α-quartz (001) silica surface (for slit width H = 20.8 Å). The silica substrate comprises two symmetric layers terminated with surface hydroxyl groups, ensuring structural and chemical symmetry along the z-axis. Confined fluids occupy the interfacial region between the hydrophilic silica and the hydrophobic graphene surfaces. Atom colors: oxygen (red), hydrogen (white), carbon (green), and ethanol hydroxyl hydrogen (cyan). To highlight surface regions, bridging oxygens and tetrahedral silicons in silica are uniformly rendered in yellow.

Table S1. Force field parameters used in the simulations.

Molecule	Site	Charge(e)	σ(Å)	ε(kcal mol^{-1})
Water	O	-0.8476	3.1655	0.1555
	H	0.4238	0	0
Ethanol	C1	0.145	3.5	0.066
	C2	-0.18	3.5	0.066
	O(C=O)	-0.683	3.12	0.17
	H	0.06	2.5	0.03
	HO(O-H)	0.418	0	0
Graphene	C	0	3.4	0.0557
Silica	S_Z	2.1	0.00000184	3.302
	O_Z	-1.05	3.1655	0.1555
	Oh	-0.95	3.1655	0.1555
	Ho	0.425	0	0
Molecule	Bond stretching	k_r(kcal mol^{-1} Å^{-2})		r_{eq}(Å)
Water	O-H			1.000
Ethanol	C-C	536		1.529
	C-H	680		1.090
	C-O	640		1.410
	O-H	1106		0.945
Silica	Oh-Ho	554.1349		1.000
Molecule	Angel stretching	k_θ(kcal mol^{-1} rad^{-2})		θ_{eq}(deg)
Water	H-O-H			109.47
Ethanol	H-C-C	75		110.7
	C-C-O	100		109.5
	H-C-H	66		107.8
	H-C-O	70		109.5
	C-O-H	70		109.5
Silica	Sz-Oh-Ho	30		109.47
Molecule	Dihedral	V_1(kcal mol^{-1})	V_2(kcal mol^{-1})	V_3(kcal mol^{-1})
Ethanol	H-C-C-O	0.0	0.0	0.468
	H-C-C-H	0.0	0.0	0.318
	C-C-O-H	0.356	0.174	0.492
	H-C-O-H	0.0	0.0	0.450

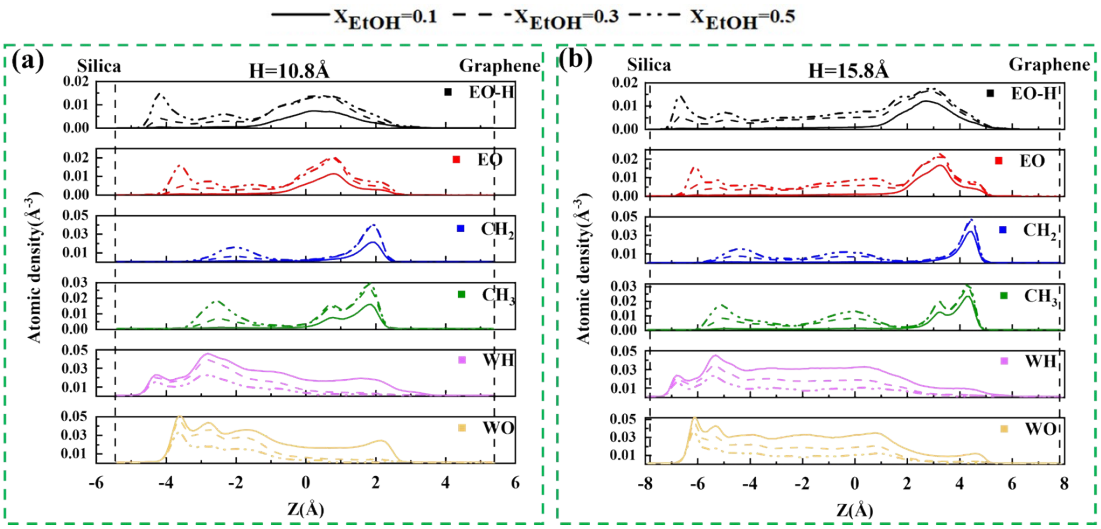

Fig. S2. Number density profiles of major functional groups in ethanol–water mixtures confined within graphene/silica nanochannels of two slit widths: (a)10.8 Å and (b) 15.8 Å. Color code: water (WO: brown, WH: purple), ethanol (EO: red, EO–H: black, CH_2: blue, CH_3: green). The solid, dashed, and dash-dotted lines correspond to ethanol mole fractions of 0.1, 0.3, and 0.5, respectively. The vertical dashed lines mark the positions of the silica (left) and graphene (right) interfaces.

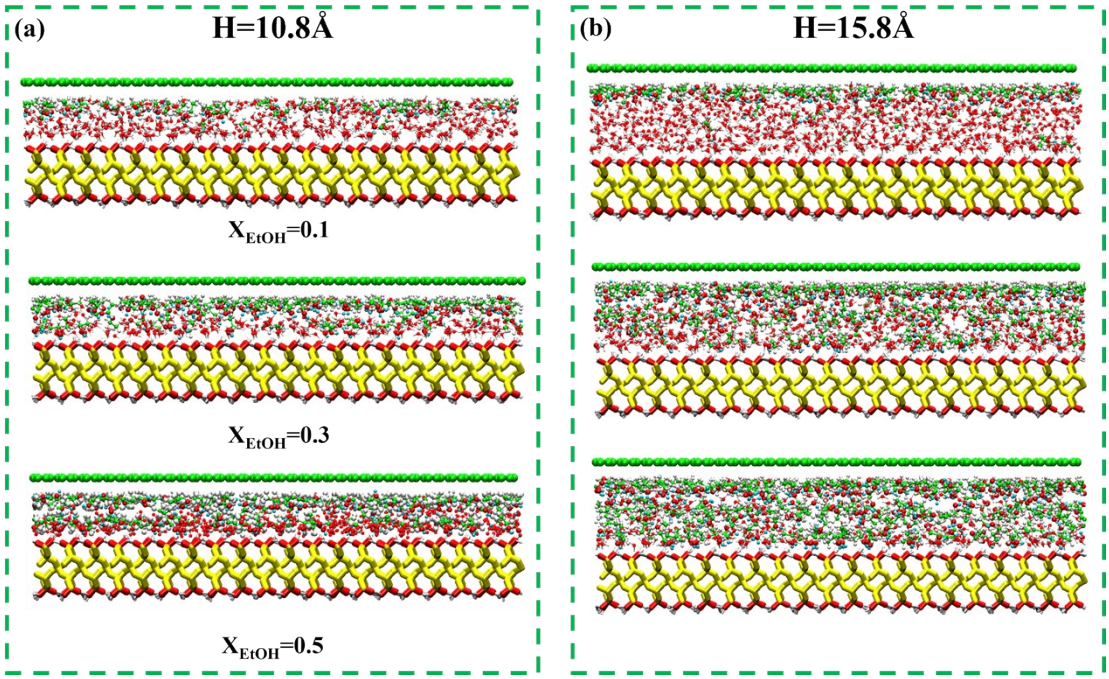

Fig. S3. Simulation snapshots at corresponding conditions for (a) 10.8 Å, (b) 15.8 Å.

Supplementary discussions for HB interaction: As a reference, we first examined the HB characteristics in the pure-component bulk systems. The simulated average water HB number is ~2.98 per water molecule, in close agreement with previously reported values of ~3.05.[1] Similarly, for the bulk ethanol, the simulated HB number is ~1.58 per ethanol molecule, consistent with the previous work.[2] For the silica-water interface, the number of HB per silanol site ranges between 0.55 and 0.67, which falls within the range reported in previous studies of water confined in SiO_2/WS_2 slit pores (0.59–0.8).[3] The results demonstrate that our simulated HB behavior is reasonable and reliable.

As shown in Figure 4c, the number of water–water HB decreases progressively with increasing ethanol concentration within the graphene/silica nanochannels, reflecting a gradual dehydration of the system.[4] In contrast, ethanol–water and ethanol–ethanol HB (Figs. 4d and 4e) become increasingly dominant, indicating that ethanol molecules are progressively integrated into the HB connectivity and contribute to the formation of alternative solvation structures.[5] Furthermore, the HB number increases with pore width across all molecular pairs, consistent with prior observations in mica–graphene slit systems.[6] This can be explained by enhanced configurational freedom and reduced confinement effects in larger pores (Figs. 3c and 3d). Notably, with increasing channel width, the number of ethanol–ethanol HBs gradually exceeds that in the bulk phase, which is likely due to the preferential accumulation of ethanol molecules near the graphene interface, facilitating HB formation with adjacent ethanol layers. Subsequently, at a pore width of 20.8 Å, a reduction in HB is observed, which can be attributed to the increased presence of ethanol molecules in the central bulk-like region of the channel, leading to a lower HB number per ethanol due to reduced local coordination.

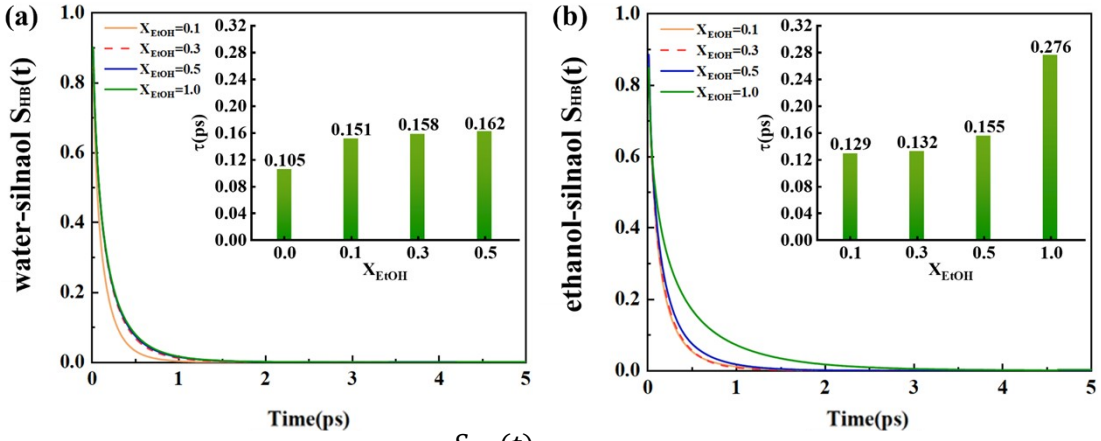

Fig. S4. HB autocorrelation functions $S_{HB}(t)$ for (a) water–silanol and (b) ethanol–silanol HB pairs at different ethanol mole fractions at H = 20.8 Å. Insets display the corresponding average HB lifetimes (τ_s^{HB}).

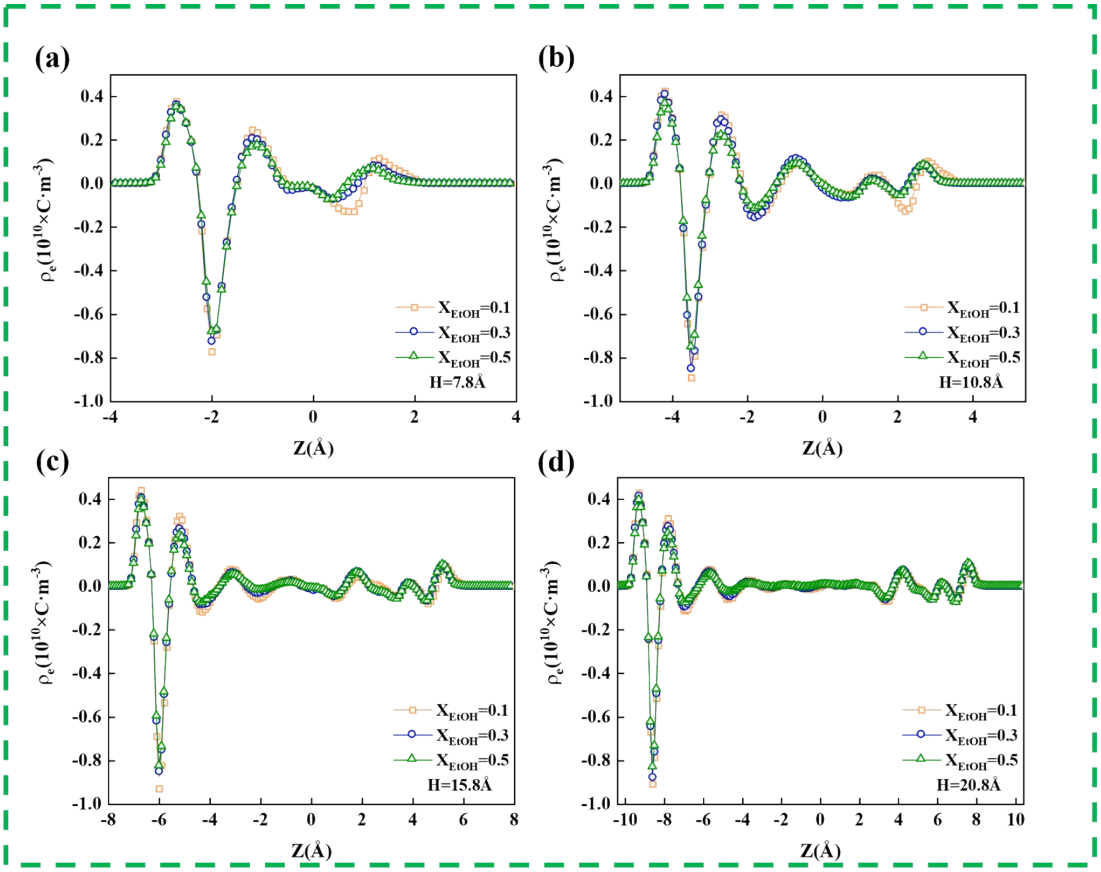

Fig. S5. Spatial profiles of perpendicular polarization density (ρ_e) within graphene–silica nanochannels under different mixture compositions. Panels (a–d) correspond to slit widths increasing from H = 7.8 to 20.8 Å.

Fig. S5 shows the asymmetric atomic charge density distributions ($\rho_e(z)$) of the mixtures confined within the graphene-silica slits. At a narrow width of 7.8 Å (Figure S5a), a pronounced positive maximum of charge density peak is observed on the silica side, corresponding to the density layers of hydrogen atoms from both ethanol and water molecules (Fig. 1a). A distinct region of negative charge density emerges adjacent to the silica surface, primarily arising from the accumulation of oxygen atoms from water and ethanol molecules. Toward the graphene side, the positive and negative extrema reflect the lower molecular density layer near the interface (Fig. 1a). As the ethanol concentration increases, the silica side feature remains nearly unchanged, owing to the density complementarity between the two components at the interface. In

contrast, on the graphene side, the charge density extrema are slightly reduced because the gradual depletion of interfacial water (Fig. 1a) diminishes the local contribution of polar species.

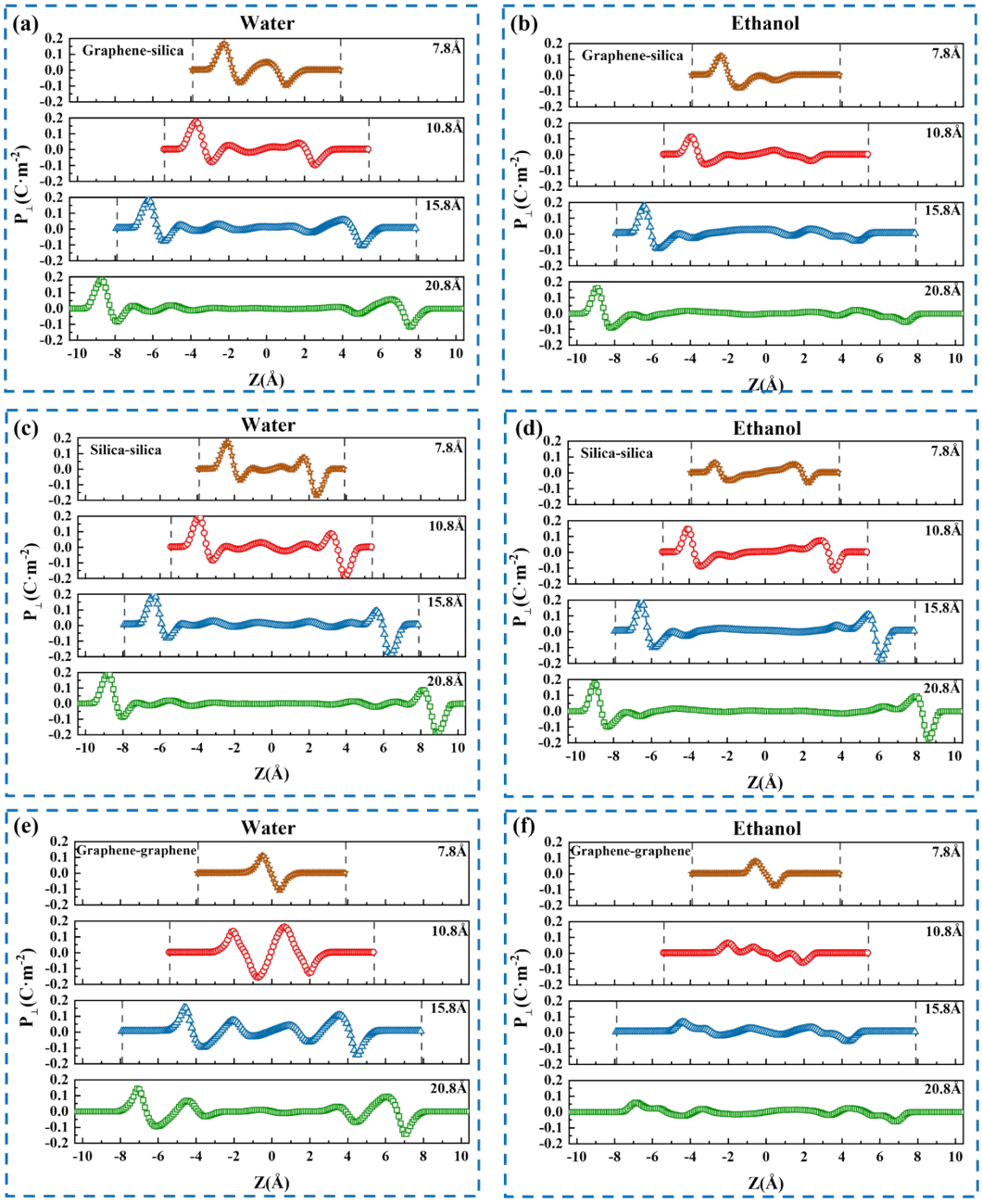

Fig. S6 Spatial profiles of perpendicular polarization density $p_{\perp}(z)$ within different nanochannels. Panels (a, b) show results for graphene-silica slits (H = 7.8 – 20.8 Å), and (c, d) for silica-silica slits (H = 7.8 – 20.8 Å). (e, f) show results for graphene-graphene slits (H = 7.8 – 20.8 Å).

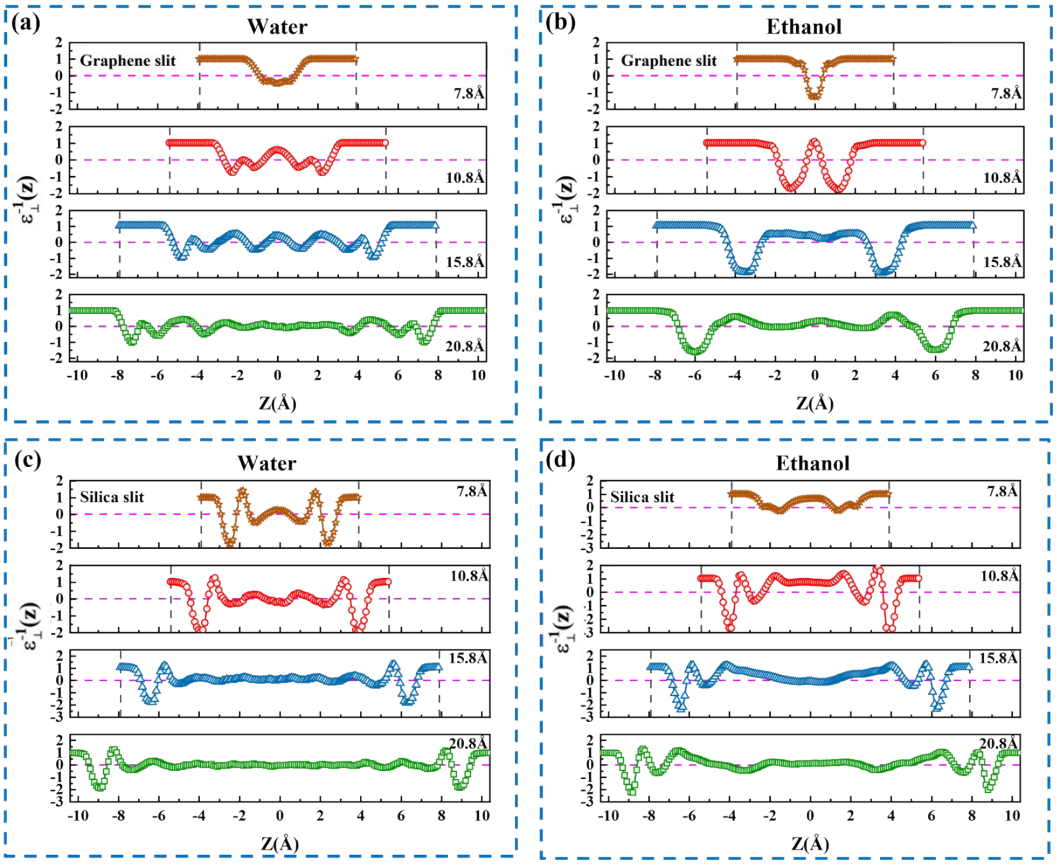

Fig. S7. Spatial profiles of the inverse perpendicular dielectric constant $\varepsilon_{\perp}^{-1}(z)$ for (a, c) pure water and (b, d) pure ethanol confined in slit pores. (a, b) correspond to graphene slits, while (c, d) correspond to silica slits. Line colors represent different slit widths. Solid markers indicate simulation results, and the horizontal magenta dashed lines denote the corresponding bulk inverse dielectric constant ($1/\varepsilon_b$). The vertical dashed lines mark the positions of the solid–liquid interfaces (graphene or silica).

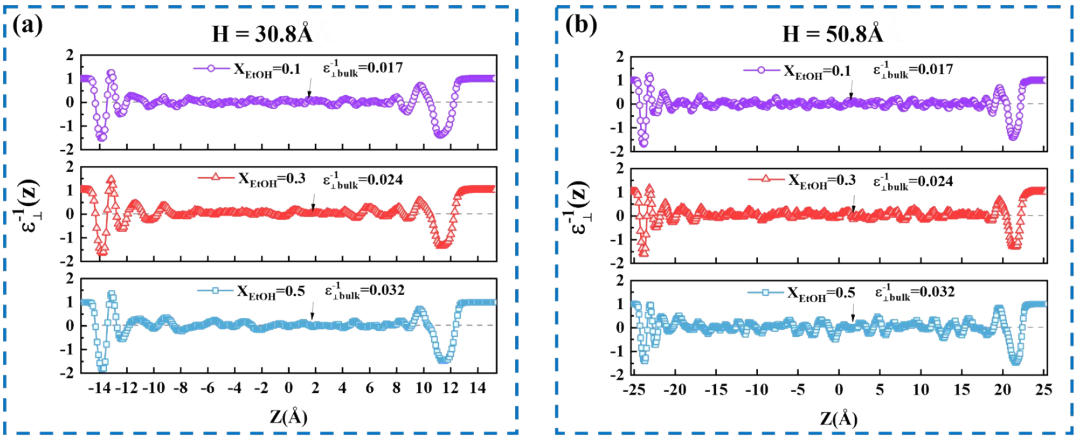

Fig. S8 Spatial profiles of the inverse perpendicular dielectric constant $\varepsilon^{-1}_{\perp}(z)$ for ethanol-water mixtures of varying compositions confined between asymmetric graphene–silica nanochannel. Horizontal dashed lines denote the inverse bulk dielectric constant.

Table S2. Dielectric constants of bulk ethanol–water mixtures at different mole fractions.

X_{EtOH}	0.0	0.1	0.3	0.5	1.0
ε_b	72.2±0.7	58.5	41.8±0.7	30.7±0.4	17.2±0.6
$\varepsilon'_{b(\text{corrected})}$	73.1±0.7	59.4	42.7±0.7	31.5±0.4	18.1±0.6
Exp. (Lit.)	78.25	66.6	47.73	36.94	24.47
Sim. (Lit.)	70.8	63.8	43.4	29.2±0.3	17.7

Table S3. Effective perpendicular dielectric constants ($\bar{\varepsilon}_{\perp}$) of pure substances and ethanol–water mixtures confined within graphene–silica, graphene-graphene and silica-silica nanochannels, at different slit widths.

Slit type	X_{EtOH}	7.8 Å	10.8 Å	15.8 Å	20.8 Å	30.8 Å	50.8 Å
graphene-silica	0	4.989	8.319	13.114	17.146	27.83	47.581
	0.1	4.309	6.105	10.336	13.182	20.951	31.493
	0.3	3.092	5.217	8.268	11.899	18.314	27.212
	0.5	2.614	5.085	7.674	10.642	16.551	21.257
	1.0	2.154	4.415	5.765	8.311	11.355	14.174
graphene-graphene	0.0	1.901	3.012	4.994	6.252	9.773	16.251
	1.0	1.739	3.574	4.917	4.949	7.461	10.211
silica-silica	0.0	4.112	7.203	9.121	11.658	17.059	26.529
	1.0	2.512	4.661	6.678	8.362	10.751	12.834

Dielectric Response of Pure Components in Symmetric and Asymmetric Nanochannels: Figure S6 presents the $p_{\perp}(z)$ of pure-component systems. For pure water, the graphene–silica channel exhibits a pronounced asymmetric polarization profile (Fig. S6a). Specifically, strong interfacial polarization arises near the silica surface due to HB interactions, whereas the response near the graphene interface is significantly weaker. This contrast between the highly polarized hydrophilic interface and the weakly polarized hydrophobic interface results in a larger net polarization contribution across the slit. In comparison, the symmetric silica channel displays strong polarization at both interfaces induced by hydrogen bonding with water molecules (Fig. S6c). However, such interactions also impose constraints on molecular fluctuations, leading to a slightly lower dielectric response than that of the hybrid channel. In contrast, the graphene-graphene slit exhibits weakened interfacial polarization due to the intrinsically weak fluid–surface interactions, resulting in a reduced dielectric response (Fig. S6e).

A different trend is observed for ethanol. In the graphene–silica channel (Fig. S6b), the hydrophobic nature of graphene reduces the interfacial orientational ordering of ethanol molecules (Fig. 3c), leading to a pronounced decrease in the peak values of $p_{\perp}(z)$. In comparison, ethanol molecules maintain a relatively high degree of interfacial

ordering in silica–silica channels, giving rise to stronger polarization and consequently a higher effective dielectric response than that of the asymmetric channel (Fig. S6d). In the graphene–graphene channel, the inherently weak fluid–surface interactions, combined with the low polarity of ethanol, further suppress interfacial polarization, resulting in the lowest dielectric response (Fig. S6e). However, with increasing slit width, bulk-like characteristics emerge earlier in the asymmetric channel, leading to a rapid increase in the dielectric response, which eventually exceeds that of the symmetric silica channel at comparable pore sizes.

Table S4. Fitted parameters from the Langevin model for different ethanol mole fractions.

Type	X_{EtOH}	Fitted parameters		Derived Quantities		
		ε_{sl}	σ_{d}(Å)	R^2	H_{sl}(Å)	λ_{b}(Å)
graphene-silica	0.0	2.188	0.770	0.976	5.82	1837.0
	0.1	2.802	1.242	0.993	6.33	2251.7
	0.3	1.876	1.280	0.991	6.35	1677.9
	0.5	1.691	1.477	0.991	6.38	1388.9
	1.0	1.744	1.884	0.975	6.72	872.0
graphene-graphene	0.0	1.49	2.93	0.990	6.32	6773.9
	1.0	2.15	4.00	0.897	7.11	1763.5
silica-silica	0.0	3.292	1.807	0.974	5.24	3966.8
	1.0	1.864	1.945	0.987	6.01	892.7

Langevin fitting of dielectric permittivity: Across all compositions. The extrapolated single-layer dielectric constant ε_{sl} falls within the range of 1–4, consistent with the expected suppression of dipolar fluctuations in molecularly thin films. The fitted effective monolayer thickness H_{sl} remains stable at approximately 5–7 Å. Interestingly, in the case of pure water, this value closely matches the sum of the distances from the graphene surface to the peak positions of the oxygen density profiles on both sides.

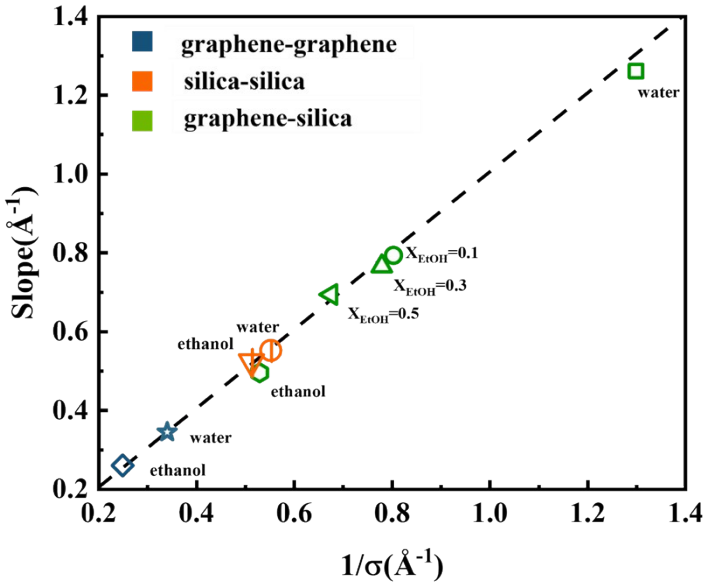

Fig. S9 Correlation between the fitted slopes and the reciprocal characteristic length ($1/\sigma_d$) for all simulated systems. Blue, orange, and green symbols correspond to graphene–graphene, silica–silica and graphene–silica nanochannels, respectively, at different ethanol mole fractions. Data for pure water and ethanol are also included. The dashed line serves as a guide to the eye.

References

1. O. Gereben and L. Pusztai, The Journal of Physical Chemistry B, 2015, 119, 3070-3084.
2. S. Y. Noskov, G. Lamoureux and B. Roux, The Journal of Physical Chemistry B, 2005, 109, 6705-6713.
3. K. L. Milton, L. Hargreaves and A. Shluger, The Journal of Physical Chemistry C, 2025, 129, 4261-4271.
4. A. Ghoufi, F. Artzner and P. Malfreyt, The Journal of Physical Chemistry B, 2016, 120, 793-802.
5. F. Pinzan, F. Artzner and A. Ghoufi, ACS Omega, 2020, 5, 25423-25431.
6. A. K. Metya, The journal of physical chemistry. B, 2022, 126, 7385-7392.